Nanoscale Advances

PAPER

View Article Online
View Journal | View Issue

Cite this: *Nanoscale Adv.*, 2023, **5**, 675

Integration of photovoltaic and photogating effects in a WSe_2/WS_2/p-Si dual junction photodetector featuring high-sensitivity and fast-response†

Zihao Huang,[ab] Yuchen Zhou,[bc] Zhongtong Luo,[b] Yibing Yang,[b] Mengmeng Yang,[d] Wei Gao,[d] Jiandong Yao,[a] Yu Zhao,[b] Yuhua Yang,*[a] Zhaoqiang Zheng*[b] and Jingbo Li[de]

Two-dimensional (2D) material-based van der Waals (vdW) heterostructures with exotic semiconducting properties have shown tremendous potential in next-generation photovoltaic photodetectors. Nevertheless, these vdW heterostructure devices inevitably suffer from a compromise between high sensitivity and fast response. Herein, an ingenious photovoltaic photodetector based on a WSe_2/WS_2/p-Si dual-vdW heterojunction is demonstrated. First-principles calculations and energy band profiles consolidate that the photogating effect originating from the bottom vdW heterojunction not only strengthens the photovoltaic effect of the top vdW heterojunction, but also suppresses the recombination of photogenerated carriers. As a consequence, the separation of photogenerated carriers is facilitated and their lifetimes are extended, resulting in higher photoconductive gain. Coupled with these synergistic effects, this WSe_2/WS_2/p-Si device exhibits both high sensitivity (responsivity of 340 mA W^{-1}, a light on/off ratio greater than 2500, and a detectivity of 3.34×10^{11} Jones) and fast response time (rise/decay time of 657/671 μs) under 405 nm light illumination in self-powered mode. Finally, high-resolution visible-light and near-infrared imaging capabilities are demonstrated by adopting this dual-heterojunction device as a single pixel, indicating its great application prospects in future optoelectronic systems.

Received 17th August 2022
Accepted 26th November 2022

DOI: 10.1039/d2na00552b

rsc.li/nanoscale-advances

1. Introduction

Benefitting from their exotic properties, including strong light–matter interactions,[1] magnificent in-plane carrier mobility,[2] atomic layer thicknesses,[3] and flexible integrability,[4] two-dimensional (2D) materials have attracted extensive attention in both academia and industry. In particular, 2D materials with naturally passivated surfaces enable the integration of any desired van der Waals (vdW) heterojunction without the compatibility and lattice matching constraints that plague 3D silicon (Si) platforms.[5–7] vdW heterojunctions combine the advantages of disparate 2D materials and endow them with more functionalities.[8,9] To date, a variety of artificial 2D vdW heterojunctions have been constructed through vdW epitaxy or layer stacking methods, such as WSe_2/Bi_2Te_3,[10] Te/In_2S_3,[11] PtS_2/WSe_2,[12] and WS_2/h-BN/$PdSe_2$.[5] These vdW heterojunctions exhibit fascinating electronic and optoelectronic properties, which hold promising applications in future optoelectronic devices, especially in photodetectors. An ideal photodetector should simultaneously possess high sensitivity (responsivity, light on/off ratio and detectivity), fast response time, and free energy consumption.[6,13] However, these reported 2D vdW heterojunction photodetectors usually suffer from an inevitable trade-off between high sensitivity and fast response time.[14] On one hand, 2D vdW heterojunction photodetectors based on the photovoltaic effect can work in self-powered mode, and the built-in fields endow the devices with high light on/off ratios and fast response time.[1,15] For example, by leveraging the type-II interfacial band offset between Bi_2O_2Se and WSe_2, the self-driven device achieves a light on/off ratio above 10^5 and a response time of 2.4 μs.[16] Unfortunately, the responsivities of these devices are always unsatisfactory due to the absence of

[a]State Key Laboratory of Optoelectronic Materials and Technologies, Nanotechnology Research Center, School of Materials Science & Engineering, Sun Yat-sen University, Guangzhou 510275, Guangdong, P. R. China. E-mail: yangyuh3@mail.sysu.edu.cn
[b]Guangdong Provincial Key Laboratory of Information Photonics Technology, School of Materials and Energy, Guangdong University of Technology, Guangzhou 510006, Guangdong, P. R. China. E-mail: zhengzhq5@mail2.sysu.edu.cn
[c]Honor Device Co.,Ltd, Shenzhen 518000, Guangdong, P. R. China
[d]Institute of Semiconductors, South China Normal University, Foshan 528225, Guangdong, P. R. China
[e]Guangdong Provincial Key Laboratory of Chip and Integration Technology, Guangzhou 510631, P. R. China

† Electronic supplementary information (ESI) available. See DOI: https://doi.org/10.1039/d2na00552b

internal gain.[9,17] On the other hand, 2D vdW heterojunction photodetectors with high responsivity are operated in photogating mode.[6] One type of photogenerated carrier acts as a local gate, which prolongs the lifetime of the other, resulting in high photogain accompanied by large dark currents and slow response times.[17,18]

To enable practical application of 2D vdW heterostructure photodetectors, considerable effort has been devoted to construct devices that simultaneously achieve high sensitivity and fast response time. For instance, the $PdSe_2/MoS_2$ junction field-effect transistor exhibits both high sensitivity (responsivity of 600 A W^{-1} and detectivity of 10^{11} Jones) and a fast response time of 100 ms through dual-gate modulation.[19] However, these studies have to introduce additional electric extra fields, leading to static power dissipation. Furthermore, thus far, investigations of photovoltaic and photogating effects in 2D vdW heterostructure photodetectors have been conducted independently since different device structures and material compositions are usually required. In addition, due to the stability and maturity of Si technology, 2D materials are unlikely to completely replace the Si market.[20,21] Therefore, it is well documented that hybrid dimensional heterostructures constructed from 2D materials and 3D Si are an effective strategy for optimizing photodetection performance.[22–24]

Herein, an ingenious photovoltaic photodetector based on a hybrid dimensional WSe_2/WS_2/p-Si dual-vdW heterojunction (named HDH) is constructed, which can realize the coupling of the photovoltaic effect and photogating effect to overcome previous limitations. In this HDH device, p-Si is floating and not connected to any electrodes, resulting in a photogating effect in the bottom WS_2/p-Si heterojunction. Such an effect not only strengthens the photovoltaic effect of the top WSe_2/WS_2 heterojunction and facilitates the separation of photogenerated carriers, but also delivers a higher photoconductive gain. Consequently, this HDH device demonstrates both high sensitivity (responsivity of 340 mA W^{-1}, a light on/off ratio greater than 2500, and a detectivity of 3.34×10^{11} Jones) and fast response time (rise/decay time of 657/671 μs) under 405 nm light illumination in self-powered mode. Specially, outstanding visible-light and near-infrared imaging capabilities of the HDH device are demonstrated, revealing the versatile roles that 2D vdW heterojunctions can play in future optoelectronic applications.

2. Results and discussion

Fig. 1 illustrates the fabrication procedure of the HDH device (details are described in the Experimental section). Briefly, the underlying p-Si is exposed by selectively etching off the oxide layer on SiO_2/p-Si. Then, WS_2 and WSe_2 flakes are exfoliated from the bulk single crystal and stacked sequentially onto the edge of the p-Si window. Next, drain (Ti/Au) and source (Au) electrodes are patterned and deposited on the WS_2 and WSe_2 flakes, respectively. The detailed preparation procedure is described in the Experimental section.

Fig. 2a shows an optical microscope image of the HDH device, where WSe_2 and WS_2 flakes are highlighted in blue and red dotted lines, respectively. High-resolution transmission electron microscope (HRTEM) images of the WS_2 and WSe_2 flakes are presented in Fig. 2b and c, respectively. Evident lattice fringes without defect atoms are observed, indicating that the flakes are well crystallized. The lattice spacing in WS_2 and WSe_2 is 0.27 nm and 0.28 nm, respectively, corresponding to the $(10\bar{1}0)$, $(01\bar{1}0)$, and $(\bar{1}100)$ planes. The fast Fourier transform (FFT) patterns in the insets of Fig. 2b and c exhibit a single set of hexagonally symmetric diffractions with sharp diffraction points, disclosing their single-crystal feature. Energy dispersive X-ray spectroscopy (EDS) characterization studies of the flakes are shown in Fig. S1.† The elemental distributions are uniform, validating the high homogeneity of the WSe_2 and WS_2 flakes. Fig. S2† shows the Raman spectra of the WSe_2/WS_2/p-Si device. The typical Raman peaks obtained for WS_2 and WSe_2 are in agreement with previously reported values.[25–27] Moreover, the Raman spectra of WSe_2/WS_2/p-Si is the sum of WSe_2 and WS_2, indicating that high quality vdW heterostructures are constructed after transfer processes.[16] In addition, the Raman peaks of WS_2 in the overlapping region are significantly quenched, which can be attributed to the interfacial coupling effect and the absorption of excitation light by top WSe_2.[17] Atomic force microscopy (AFM) measurements for the WSe_2 and WS_2 flakes are shown in Fig. 2d, and the thicknesses of WS_2 and WSe_2 are obtained as 76.4 nm and 79.1 nm, respectively. Fig. 2e and f show the Kelvin probe force microscope (KPFM) images obtained from the interfaces of WS_2/p-Si and WSe_2/WS_2, respectively. The Fermi level difference (ΔE_f) between WSe_2 and WS_2 is calculated to be 25.6 meV, and the ΔE_f between WS_2 and p-Si is up to 109.1 meV (detailed calculation process is described in Note S1†).

Afterward, optoelectronic performance of the WSe_2/WS_2/p-Si device is systematically characterized. Fig. 3a depicts the electrical connections of the device, where D and S denote the drain and source, respectively. Fig. 3b shows the PL spectra recorded from different areas. Both the WS_2 and WSe_2 present two PL peaks, which are located at around 650 nm and 863 nm (for WS_2), and 780 nm and 893 nm (for WSe_2). These peaks can be related to the direct and indirect band excitation in multilayered WS_2 and WSe_2.[28,29] In the overlapping region, the PL peaks exhibit obvious quenching and a slight redshift, manifesting the efficient separation of photogenerated carriers in the WSe_2/WS_2/p-Si device.[10,30,31] The spectral photoresponse of the HDH device shown in Fig. 3c reveals that the device demonstrates a broadband photosensitivity from the visible to the near-infrared region. In addition, the HDH device shows two photoresponse peaks at 630 nm and 765 nm, which corresponded to the photoresponse peaks of WS_2 and WSe_2 (Fig. S2†). Due to the low responsivity of the Si device and the photoresponse peak at 965 nm (Fig. S3†), it can be inferred that the photogenerated carriers in the WSe_2/WS_2/p-Si device are mainly generated from the WSe_2 and WS_2 layers. The current *versus* voltage (*I*–*V*) curves of the HDH device in the dark and under 405 nm light (102.69 mW cm^{-2}) are demonstrated in Fig. 3d. The counterpart devices with other architectures are also measured for comparison, as shown in Fig. S5 and S6.† Under dark, pronounced rectifying behavior is observed in the HDH and WS_2/p-Si devices. The

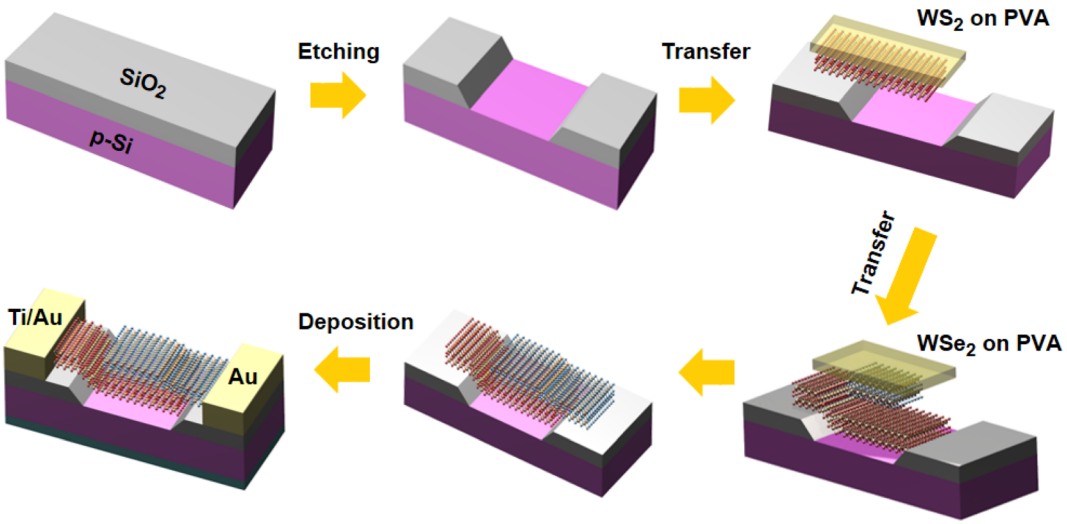

Fig. 1 Schematic drawing of the fabrication procedure of the HDH device.

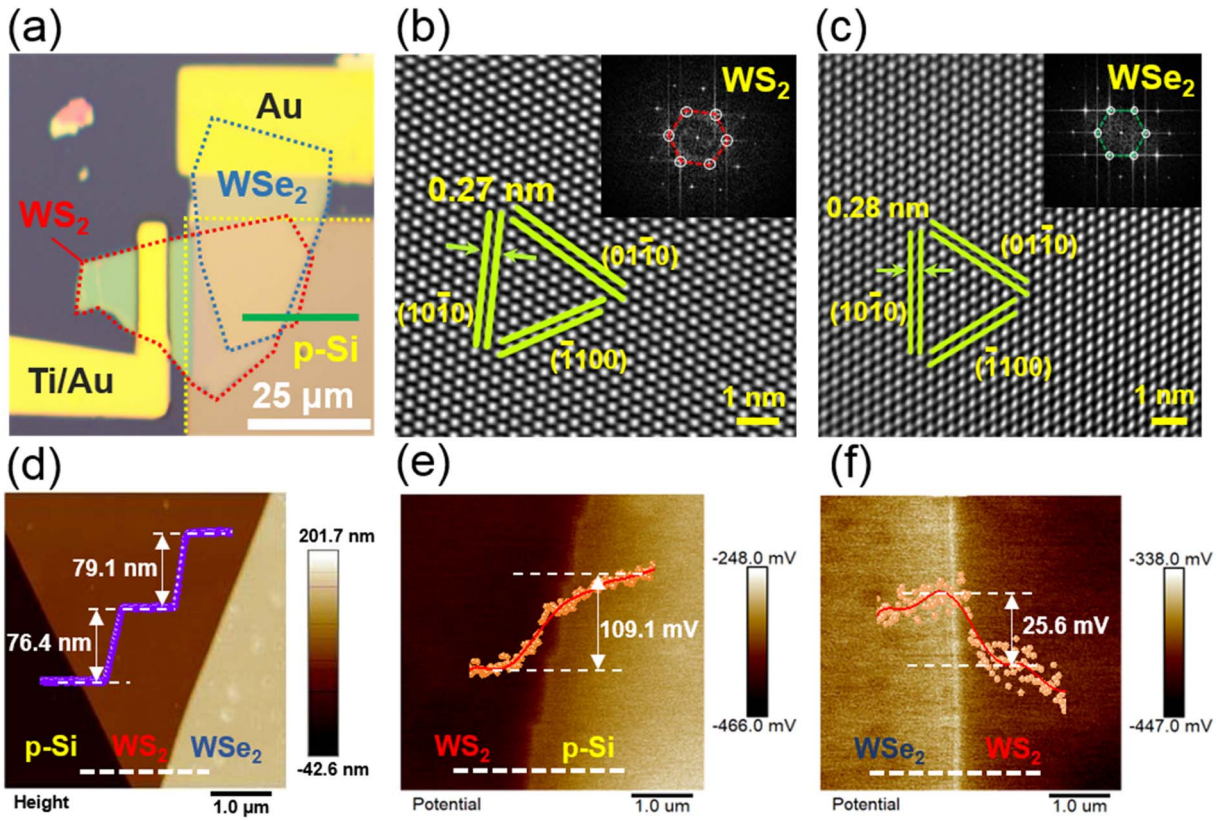

Fig. 2 Structural properties of the HDH photodetector. (a) Optical micrograph of the HDH device. The WSe_2 and WS_2 flakes are highlighted in blue and red dotted lines, respectively. (b and c) HRTEM images of WS_2 and WSe_2 and the insets show the corresponding FFT patterns, respectively. (d) AFM image measured at the green solid line in (a). The inset shows the height profile across the white line in (d). The thicknesses of WS_2 and WSe_2 are 76.4 nm and 79.1 nm, respectively. KPFM images obtained from the interfaces of (e) WS_2/p-Si and (f) WSe_2/WS_2. The inset shows the potential profiles across the corresponding white lines. The potential difference between WS_2 and p-Si is 109.1 mV, and the potential difference between WSe_2 and WS_2 is 25.6 mV.

measured results (Fig. S7 and S8†) and widely reported results[32,33] show that both Au-WSe_2 and Ti/Au-WS_2 are ohmic contacts. Therefore, this rectification behavior indicates the formation of a built-in electric field in the device. Besides, the minimum dark current is not at $V_{ds} = 0$ V, which can be attributed to the surface adsorption of the channel. The absorbate induces charge injection into the channel, which increases the dark current. At a small reverse bias, the carrier

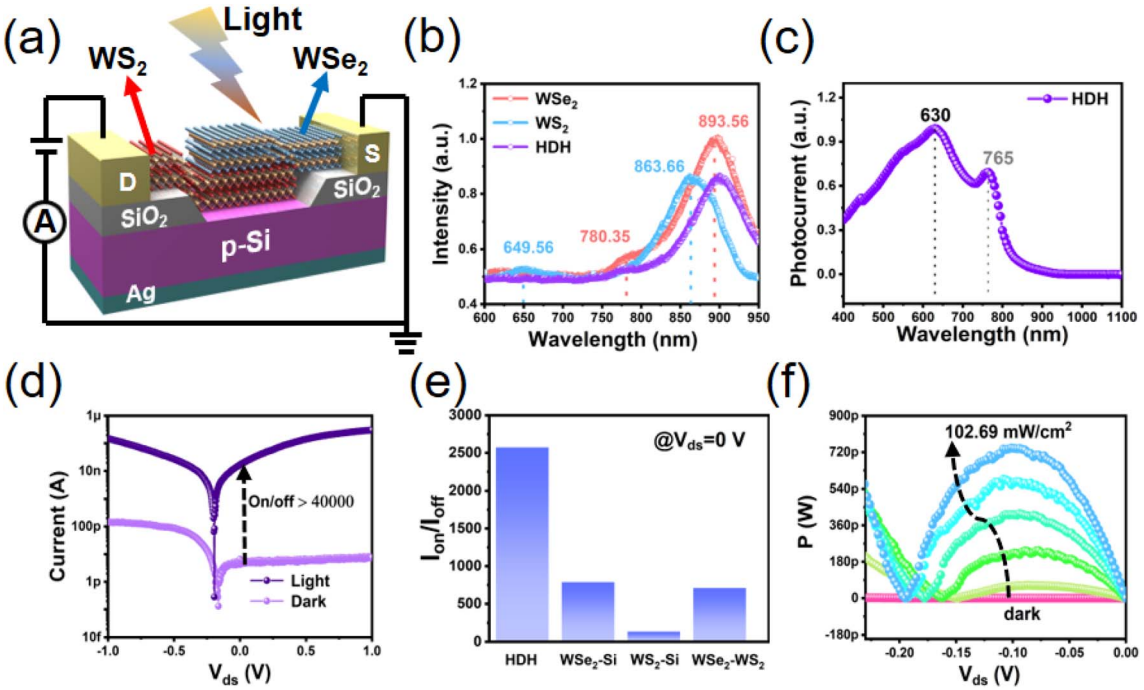

Fig. 3 Optoelectronic characteristics of the HDH photodetector. (a) Electrical connections of the device. (b) PL spectra collected from WSe_2, WS_2, and HDH. (c) Spectral photoresponse of the device under the illumination of 400–1100 nm light. (d) *I*–*V* curves in the dark and under 405 nm light (102.69 mW cm^{-2}). The maximum light on/off ratio exceeds 40 000. (e) Comparison of the light on/off ratio of the devices with different architectures at a bias of 0 V. (f) Plots of electrical power under different intensities of 405 nm light.

diffusion increases and recombines with the injected charge, reducing the dark current. At high reverse bias, the diffusion current dominates, and the dark current increases rapidly. This phenomenon is also observed in other 2D material devices.[12,34,35] Under 405 nm light illumination, the HDH device exhibits an obvious photoresponse, and the maximum light on/off ratio (defined in Note S2†) exceeds 40 000. Moreover, the light on/off ratio of the HDH device is still greater than 2500 at 0 V bias, showing excellent self-powered photodetection properties. Fig. 3e compares the light on/off ratio at 0 V bias for devices with different architectures, which shows that our dual-heterostructure device exhibits clear advantages. In addition, the light on/off ratio of the WS_2/p-Si device is lower than that of the WSe_2/p-Si device. In the WS_2/p-Si device, the top WSe_2 layer is not connected to the circuit. As a result, the electron–hole pairs generated in WSe_2 cannot be effectively converted into photocurrent, which makes the photocurrent of the WS_2/p-Si device much lower than that of the WSe_2/p-Si device. Fig. 3f presents the photovoltaic characteristics of the HDH device under different intensities of 405 nm light. The maximum open-circuit voltage (V_{oc}) is 0.19 V and the maximum output electrical power (P_{el}, $P_{el} = I_{ds} \times V_{ds}$) is 740 pW. To further increase the output power, more work will be carried out, such as optimizing electrode contact and channel thickness.

Then, photodetection metrics of the HDH device in self-powered mode are systemically investigated under 405 nm light illumination. These metrics include responsivity (R), detectivity (D^*), photoconductive gain (Gain), light on/off ratio (I_{on}/I_{off}) and response time, and their detailed calculation process is described in Note S2.† Based on the *I*–*V* curves shown in Fig. S5d–f and S6,† the power-dependent photocurrents of devices with different architectures are extracted and displayed in Fig. 4a and S5g–i.† These photocurrents are positively related to the incident light power, since the number of photogenerated carriers increases with the incident photons. Furthermore, the power density (P) dependent photocurrent (I_{ph}) follows a power-law relationship ($I_{ph} \propto P^{\alpha}$). The power factors, α, are calculated to be 0.77, 0.65, 0.24 and 0.48 for the HDH, WSe_2–WS_2, WSe_2/p-Si and WS_2/p-Si devices, respectively. The highest α of the HDH device indicates that the dual-vdW heterojunction structure can effectively reduce the recombination rate of the photoexcited carriers.[45,46] Fig. 4b–d compare the light intensity dependent responsivity, detectivity, photoconductive gain and light on/off ratio of the HDH device and conventional WSe_2–WS_2 device. Notably, all of these metrics show a decreasing tendency with increasing light intensity. Under intense light illumination, the photosensitive state of the device tends to saturate, which increases the recombination of photogenerated carriers. This phenomenon is widely observed in 2D material devices.[45,47,48] Under a relatively weak light intensity of 150 μW cm^{-2}, the HDH device achieves high sensitivity (responsivity of 340 mA W^{-1}, a detectivity of 3.34×10^{11} Jones, a Gain of nearly 1, and a light on/off ratio greater than 2500). These values are much superior to those of the conventional WSe_2–WS_2 device. Besides, Fig. 4e presents the comparison of R and D^* of our HDH device against those of other reported self-driven devices. Obviously, the performance of our HDH device takes the lead, revealing the advantage of this dual-vdW heterojunction architecture. In

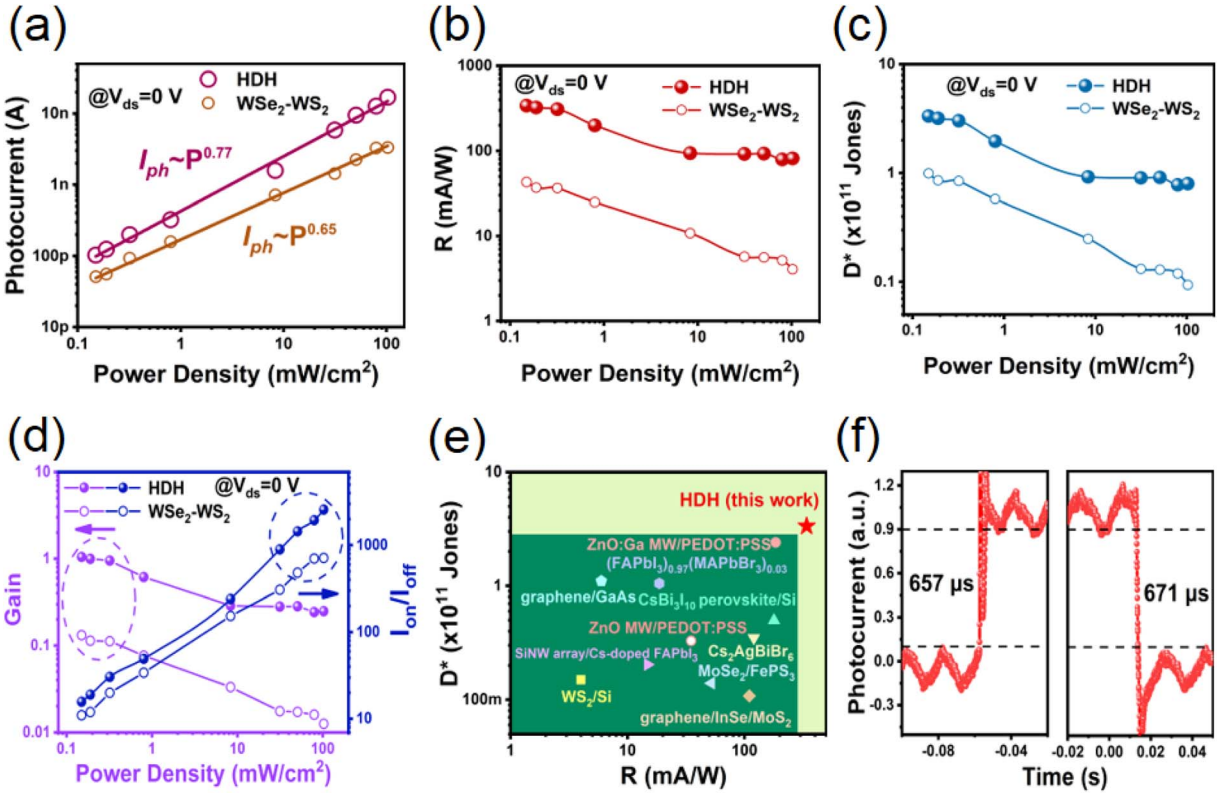

Fig. 4 Photodetection metrics of the HDH device in self-powered mode. Calculated (a) photocurrent, (b) responsivity, (c) detectivity, and (d) photoconductive gain of the HDH and WSe_2–WS_2 devices as functions of incident power density at a bias of 0 V. (e) Comparison of R and D^* of the HDH device against those of other reported self-driven devices at 0 V bias, including $Cs_2AgBiBr_6$,[36] graphene/GaAs,[37] WS_2/Si,[38] graphene/InSe/MoS_2,[39] ZnO MW/PEDOT:PSS,[40] ZnO:Ga MW/PEDOT:PSS,[40] $CsBi_3I_{10}$ perovskite/Si,[41] $(FAPbI_3)_{0.97}(MAPbBr_3)_{0.03}$,[42] $MoSe_2$/$FePS_3$,[43] and Si NW array/Cs-doped $FAPbI_3$.[44] (f) Response time of the HDH device at a bias voltage of 0 V.

addition, Fig. S9† compares the photodetection metrics of the HDH device under different bias voltages. The photoresponse properties are enhanced at positive bias and weakened at reverse bias, which is in good agreement with the reported behavior of p–n junction devices.[16,49,50] Therefore, this HDH device does not work in transistor mode, but works in photovoltaic diode mode.

Sequentially, response time represents the ability of a device to track rapidly changing optical signals. Fast response time is important for a wide range of applications including image sensing, optical communications, and so on.[51] Fig. 4f shows the transient photoresponse of the HDH device to a 405 nm pulsed light. The rise time (τ_{rise}) and decay time (τ_{decay}) are deduced to be 657 μs and 671 μs, respectively. This response time is not only significantly faster than that of the counterpart WSe_2–WS_2 device (Fig. S6c and d†), but also faster than those of most devices reported in the literature (≥4 ms).[52–57] Fig. S10† presents the time-dependent photoresponse of the HDH device under periodical 405 nm light stimulations. As can be seen, the photocurrent rapidly increases to its maximum value when the light is on, and it quickly returns to the dark state when the light is off. Moreover, the photocurrent remains almost unchanged after more than 300 photoswitching cycles, indicating the outstanding reproducibility and durability of the HDH device.

Then, the underlying operation mechanism for the excellent photoresponse properties of the HDH device is investigated. First, first-principles calculations are carried out (calculation process is available in Note S3†). Fig. 5a and b show the band decomposed charge densities for the conduction band minimum (CBM) and valence band maximum (VBM), respectively. Both of the lowest-energy holes and electrons are located on the bottom p-Si layer, indicating the strong interfacial coupling effect, which corresponds to the large ΔE_f between WS_2 and p-Si in Fig. 2e. To further analyze the charge transfer behavior in the WSe_2/WS_2/p-Si structure, the charge density difference (CDD) and the plane-averaged charge density difference ($\Delta\rho$) along the z direction are calculated and presented in Fig. 5c and d. In Fig. 5c, the yellow and cyan areas denote the electron accumulation and depletion, respectively, visually demonstrating the charge transfer at the two heterointerfaces. In Fig. 5d, the difference in electronegativity at the two heterointerfaces reveals that WSe_2 and p-Si lose electrons, suggesting that the formation of a WSe_2/WS_2/p-Si dual-heterojunction can effectively promote the spatial separation of charge carriers. Based on the above analysis and by referring to other literature reports,[21,38,58] energy band structures of the WSe_2/WS_2/p-Si structure are shown in Fig. 5e, where two type-II band alignments (staggered gap) are observed. Based on the Fermi level difference, two depletion regions and two oppositely directed

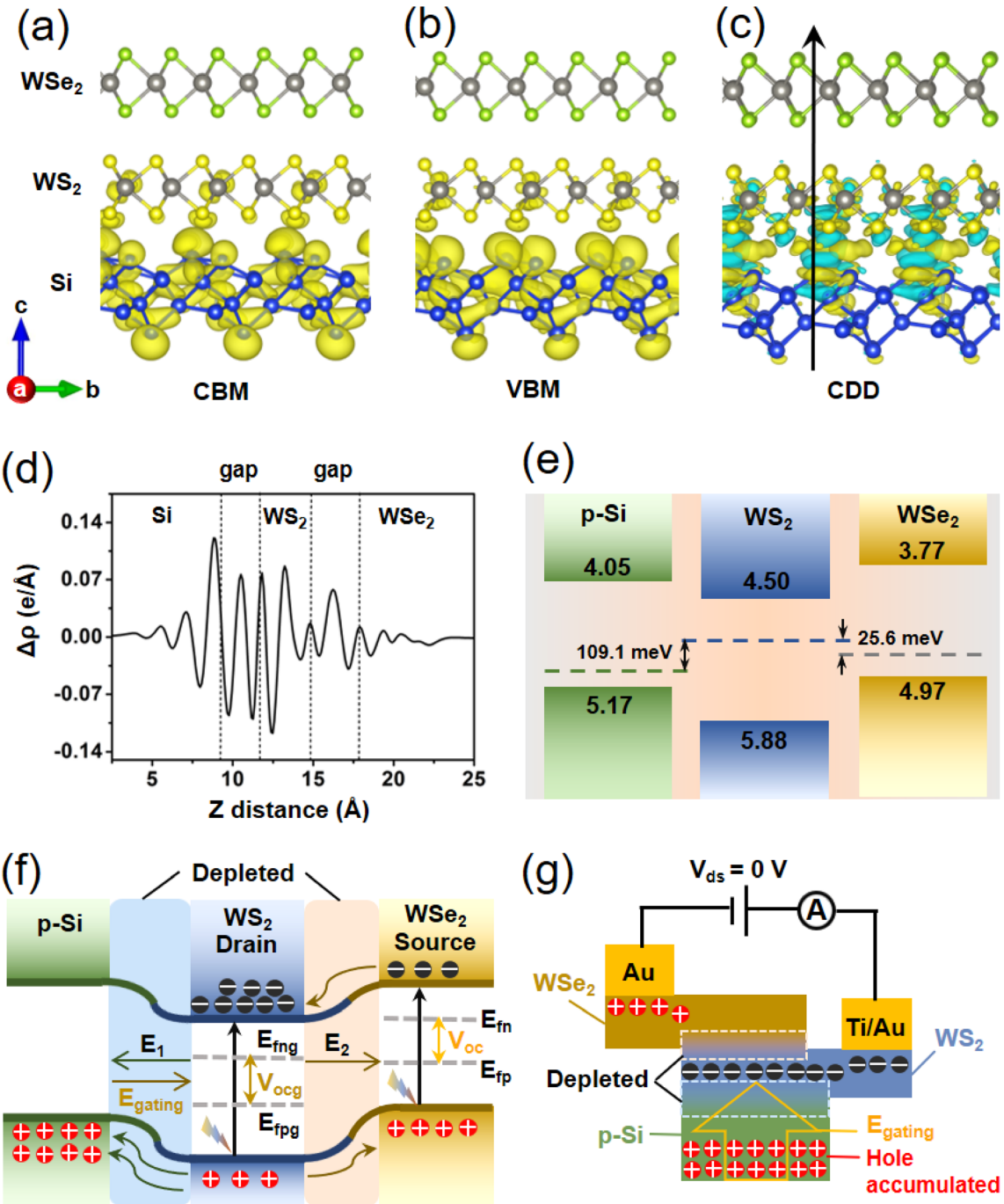

Fig. 5 Working mechanism of the HDH photodetector. Band decomposed charge density in the WSe_2/WS_2/p-Si dual heterojunctions for (a) CBM and (b) VBM. (c) Charge density difference in the WSe_2/WS_2/p-Si dual heterojunctions. The yellow and cyan areas indicate electron accumulation and depletion, respectively. (d) Plane-averaged charge density difference along the *z* direction (black line in panel c). Positive and negative values represent electron accumulation and depletion, respectively. (e) Schematic diagram of the energy band structures of WSe_2/WS_2/p-Si before contact. (f) Band alignments and charge transfer of the dual junction device under illumination. (g) Cross-sectional diagram of the HDH device. The electrodes extract photoexcited carriers and generate photocurrent. Photoexcited holes accumulated in p-Si will generate the E_{gating}.

built-in electric fields (E_1 and E_2) are formed, as depicted in Fig. S11.† Thereinto, the E_1 will be larger than E_2 due to the higher ΔE_f at the WSe_2/p-Si interface.[59] In addition, these two depletion regions will turn the sandwiched WS_2 into a high resistance region, which is beneficial to obtain low dark current. When light irradiates the HDH device, electron–hole pairs are excited in the WSe_2 and WS_2 layers (black arrows in Fig. 5f). Driven by the opposite E_1 and E_2, the photoexcited electrons in the conduction band of top WSe_2 will be swept into the sandwiched WS_2, while the photoexcited holes in the valence band of WS_2 are divided into WSe_2 and p-Si. Since E_1 is larger than E_2, more photoexcited holes will be transferred to p-Si. The

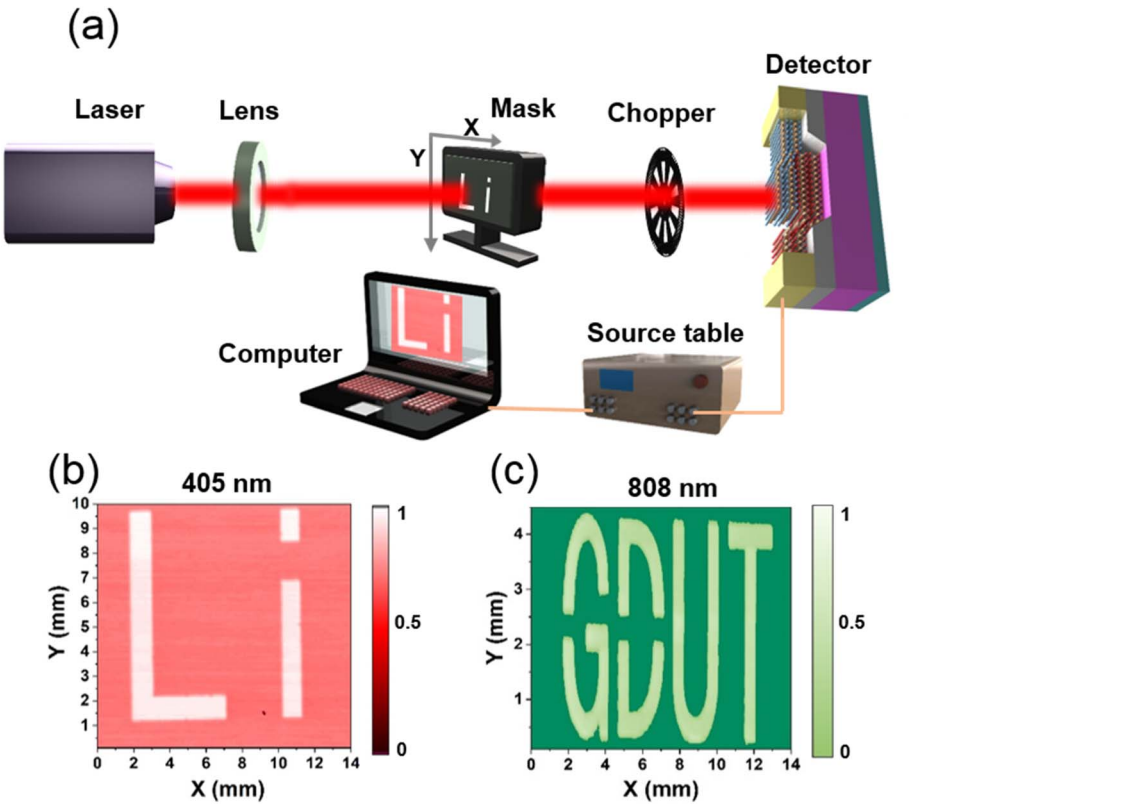

Fig. 6 Imaging application of the HDH device. (a) Schematic diagram of the measurement system for visible-NIR single-pixel imaging applications. (b) The resulting image of "Li" under 405 nm light illumination. (c) The resulting image of "GDUT" under 808 nm light illumination.

segregation of photoexcited carriers at the WS_2/p-Si interface splits the Fermi level into two quasi-Fermi levels (E_{fp} and E_{fn} in Fig. 5f), resulting in an open circuit voltage (V_{oc} in Fig. 5f). Meanwhile, as depicted in Fig. 5g, the source and drain electrodes come into contact with WSe_2 and WS_2, respectively, which extract the photoexcited carriers and generate self-powered photocurrent. Besides, the bottom p-Si is floating without connecting electrodes. Thus, the photoexcited holes in p-Si are accumulated, which generates another built-in electric field (E_{gating}), as shown in Fig. 5f and g. E_{gating} provides a photogating effect to the middle WS_2, forming an additional open circuit voltage (V_{gating} in Fig. 5f and g), which strengthens the photovoltaic effect of the top vdW heterojunction and enhances the photocurrent.[27,60] Moreover, photoexcited holes are trapped in p-Si suppressing the recombination of photogenerated carriers. Besides, the defect states on the surface of crystalline p-Si are much less than those of amorphous SiO_2, which reduces the memory effects originating from the traps and speeds up the response time.

Considering the high sensitivity of the HDH device in the visible to near-infrared region, its image sensing capability is further investigated using a single-pixel scanning imaging system. Fig. 6a schematically illustrates the measurement setup, which mainly consists of three components, namely a sensing pixel, a mask, and a light source. Here, the HDH device is used as an individual sensing pixel, hollow masks with "Li" and "GDUT" patterns can be moved along the *X*–*Y* directions controlled by a computer, and lasers with wavelengths of 405 nm and 808 nm are used as light sources. A light beam passing through the hollowed-out pattern would illuminate the HDH device, producing a higher current. With the movement of the mask, the current of the HDH device is synchronously recorded by the source table, producing a position-dependent current mapping image. As demonstrated in Fig. 6b and c, both of the resulting "Li" and "GDUT" images generated under visible (405 nm) and near-infrared (808 nm) illumination are legible with large contrast. This result reveals that the HDH device holds great potential for high-resolution imaging applications.

3. Conclusion

In summary, we have proposed a mixed-dimensional WSe_2/WS_2/p-Si dual-vdW heterojunction to achieve high sensitivity and fast response simultaneously. In self-powered mode, the device delivers a responsivity of 340 mA W^{-1}, a light on/off ratio greater than 2500, a detectivity of 3.34×10^{11} Jones and a rise/decay time of 657/671 μs under 405 nm light illumination. First-principles calculations and energy band profiles confirm that the photogating effect stemming from the floating vdW heterojunction facilitates the separation of photogenerated carriers in the other vdW heterojunctions, resulting in high performance. Moreover, high-resolution visible and near-infrared image sensors based on this WSe_2/WS_2/p-Si device have been further demonstrated, which verifies its outstanding imaging

capability. These results signify the versatility of the dual-vdW heterojunction architecture, showing bright prospects for future optoelectronic systems.

4. Experimental section

4.1 Device fabrication

The HDH device was constructed on a SiO_2/Si wafer (p-Si resistivity: 1–10 Ω cm^{-2} and SiO_2 thickness: 300 nm). Firstly, a photoresist (ARP-5350) purchased from Taizhou SUNANO New Energy Co., Ltd. was spin-coated onto the wafer and then baked at 100 °C for 4 minutes. Next, a square window (100 × 100 μm) was defined on the photoresist using a maskless UV lithography machine (purchased from TuoTuo Technology (Suzhou) Co., Ltd). Then, the processes of reactive ion etching (RIE, Oxford Estrals) were conducted to etch out the SiO_2 layer within the square window and the p-Si at the bottom was revealed. Secondly, with the help of polyvinyl alcohol (PVA), a WS_2 flake mechanically stripped from the bulk WS_2 crystal (purchased from Shanghai OnWay Technology Co., Ltd.) was transferred to the edge of the square window. Next, a mechanically exfoliated WSe_2 flake was transferred onto the WS_2/Si heterostructure arranged using an optical microscope. Thereafter, electrical contacts on the WS_2 (Ti/Au, 10/60 nm) and WS_2 (Au, 70 nm) flakes were produced by alternating UV lithography and lift-off processes. The Ag electrode (100 nm) on the back of the Si was produced by sputtering. Finally, the device was annealed at 150 °C for 1.5 hours to eliminate stresses and contaminants.

4.2 Device characterization

Morphology of the device was observed using a microscope (Motic, BA310Met), and lattice structures and elemental compositions of the WS_2 and WSe_2 flakes were characterized using a TEM system (FEI, Thermo Talos F200S). The AFM and KPFM images were taken on a scanner-probe microscope (Bruker, Dimension FastScan). PL and Raman measurements were performed on a confocal microscope (HORIBA Jobin Yvon, LabRAM HR Evolution) under a 532 nm laser stimulation. The electric and optoelectronic measurements were performed by using a Keithley 2636b source table combined with a probe station. The light sources included a 405 nm laser (CNIlaser), an 808 nm laser (CNIlaser) and a tungsten bromide bulb (Zolix), whose powers were calibrated through a power meter (Thorlabs, S120VC). High-resolution response speed was recorded through an oscilloscope (Tektronix, DPO4102B).

Author contributions

Z. Zheng and Y. Yang: project administration. Z. Huang: methodology and writing-original draft. Y. Zhou and Z. Luo: investigation. Y. Yang and M. Yang: software. W. Gao, J. Yao and Y. Zhao: writing-review & editing. J. Li: resources.

Conflicts of interest

The authors declare no competing financial interests.

Acknowledgements

This work was supported by the National Natural Science Foundation of China (62175040, 61805044, and 62004071), the Science and Technology Program of Guangzhou (202201010242), Guangdong Provincial Key Laboratory of Information Photonics Technology (2020B121201011) and "The Pearl River Talent Recruitment Program" (2019ZT08X639). The authors wish to thank Lin Liu from State Key Laboratory of Optoelectronic Materials and Technologies, Sun Yat-sen University for device construction. The authors also wish to thank Dr Xueyan Wu from the Analysis and Test Center, the Guangdong University of Technology for the structural analysis of the specimens.

References

1 M. Long, P. Wang, H. Fang and W. Hu, Progress, Challenges, and Opportunities for 2D Material Based Photodetectors, *Adv. Funct. Mater.*, 2018, **29**(19), 1803807.
2 X. Cui, G.-H. Lee, Y. D. Kim, G. Arefe, P. Y. Huang, C.-H. Lee, D. A. Chenet, X. Zhang, L. Wang, F. Ye, F. Pizzocchero, B. S. Jessen, K. Watanabe, T. Taniguchi, D. A. Muller, T. Low, P. Kim and J. Hone, Multi-terminal transport measurements of MoS_2 using a van der Waals heterostructure device platform, *Nat. Nanotechnol.*, 2015, **10**(6), 534–540.
3 N. Huo and G. Konstantatos, Recent Progress and Future Prospects of 2D-Based Photodetectors, *Adv. Mater.*, 2018, **30**(51), 1801164.
4 Y. Zhou, Y. Nie, Y. Liu, K. Yan, J. Hong, C. Jin, Y. Zhou, J. Yin, Z. Liu and H. Peng, Epitaxy and Photoresponse of Two-dimensional GaSe Crystals on Flexible Transparent Mica Sheets, *ACS Nano*, 2014, **8**(2), 1485–1490.
5 Y. Chen, Y. Wang, Z. Wang, Y. Gu, Y. Ye, X. Chai, J. Ye, Y. Chen, R. Xie, Y. Zhou, Z. Hu, Q. Li, L. Zhang, F. Wang, P. Wang, J. Miao, J. Wang, X. Chen, W. Lu, P. Zhou and W. Hu, Unipolar barrier photodetectors based on van der Waals heterostructures, *Nat. Electron.*, 2021, **4**(5), 357–363.
6 F. Wu, Q. Li, P. Wang, H. Xia, Z. Wang, Y. Wang, M. Luo, L. Chen, F. Chen, J. Miao, X. Chen, W. Lu, C. Shan, A. Pan, X. Wu, W. Ren, D. Jariwala and W. Hu, High efficiency and fast van der Waals hetero-photodiodes with a unilateral depletion region, *Nat. Commun.*, 2019, **10**(1), 4663.
7 J. Lu, J. Yan, J. Yao, Z. Zheng, B. Mao, Y. Zhao and J. Li, All-Dielectric Nanostructure Fabry-Pérot-Enhanced Mie Resonances Coupled with Photogain Modulation toward Ultrasensitive In_2S_3 Photodetector, *Adv. Funct. Mater.*, 2021, **31**(8), 2007987.
8 X. Zhou, X. Hu, J. Yu, S. Liu, Z. Shu, Q. Zhang, H. Li, Y. Ma, H. Xu and T. Zhai, 2D Layered Material-Based van der Waals Heterostructures for Optoelectronics, *Adv. Funct. Mater.*, 2018, **28**(14), 1706587.
9 M. Brandbyge, J.-L. Mozos, P. Ordejón, J. Taylor and K. Stokbro, Density-functional method for nonequilibrium electron transport, *Phys. Rev. B: Condens. Matter Mater. Phys.*, 2002, **65**(16), 165401.

10 H. Liu, X. Zhu, X. Sun, C. Zhu, W. Huang, X. Zhang, B. Zheng, Z. Zou, Z. Luo, X. Wang, D. Li and A. Pan, Self-Powered Broad-band Photodetectors Based on Vertically Stacked WSe_2/Bi_2Te_3 p–n Heterojunctions, *ACS Nano*, 2019, **13**(11), 13573–13580.

11 X. Cao, Z. Lei, B. Huang, A. Wei, L. Tao, Y. Yang, Z. Zheng, X. Feng, J. Li and Y. Zhao, Non-Layered Te/In_2S_3 Tunneling Heterojunctions with Ultrahigh Photoresponsivity and Fast Photoresponse, *Small*, 2022, **18**(18), e2200445.

12 C. Tan, S. Yin, J. Chen, Y. Lu, W. Wei, H. Du, K. Liu, F. Wang, T. Zhai and L. Li, Broken-Gap PtS_2/WSe_2 van der Waals Heterojunction with Ultrahigh Reverse Rectification and Fast Photoresponse, *ACS Nano*, 2021, **15**(5), 8328–8337.

13 Y. Jiang, R. Wang, X. Li, Z. Ma, L. Li, J. Su, Y. Yan, X. Song and C. Xia, Photovoltaic Field-Effect Photodiodes Based on Double van der Waals Heterojunctions, *ACS Nano*, 2021, **15**(9), 14295–14304.

14 N. Huo and G. Konstantatos, Ultrasensitive all-2D MoS_2 Phototransistors Enabled by an Out-of-plane MoS_2 PN Homojunction, *Nat. Commun.*, 2017, **8**(1), 572.

15 Z. Q. Zheng, J. D. Yao, L. Zhu, W. Jiang, B. Wang, G. Yang and J. Li, Tin Dioxide Quantum Dots Coupled with Graphene Enabled High-performance Bulk-silicon Schottky Photodetector, *Mater. Horiz.*, 2018, **5**(4), 727–737.

16 P. Luo, F. Wang, J. Qu, K. Liu, X. Hu, K. Liu and T. Zhai, Self-Driven WSe_2/Bi_2O_2Se van der Waals Heterostructure Photodetectors with High Light On/Off Ratio and Fast Response, *Adv. Funct. Mater.*, 2020, **31**(8), 2008351.

17 X. Zhou, X. Hu, S. Zhou, H. Song, Q. Zhang, L. Pi, L. Li, H. Li, J. Lü and T. Zhai, Tunneling Diode Based on WSe_2/SnS_2 Heterostructure Incorporating High Detectivity and Responsivity, *Adv. Mater.*, 2018, **30**(7), 1703286.

18 J. Lu, Z. Zheng, J. Yao, W. Gao, Y. Zhao, Y. Xiao and J. Li, 2D In_2S_3 Nanoflake Coupled with Graphene toward High-Sensitivity and Fast-Response Bulk-Silicon Schottky Photodetector, *Small*, 2019, **15**(47), 1904912.

19 H. Wang, Z. Li, D. Li, X. Xu, P. Chen, L. Pi, X. Zhou and T. Zhai, Junction Field-Effect Transistors Based on $PdSe_2/MoS_2$ Heterostructures for Photodetectors Showing High Responsivity and Detectivity, *Adv. Funct. Mater.*, 2021, 2106105.

20 W. Yang, J. Chen, Y. Zhang, Y. Zhang, J. H. He and X. Fang, Silicon-Compatible Photodetectors: Trends to Monolithically Integrate Photosensors with Chip Technology, *Adv. Funct. Mater.*, 2019, **29**(18), 1808182.

21 Z. Zheng, J. Yao, B. Wang, Y. Yang, G. Yang and J. Li, Self-Assembly High-Performance UV-vis-NIR Broadband beta-In_2Se_3/Si Photodetector Array for Weak Signal Detection, *ACS Appl. Mater. Interfaces*, 2017, **9**(50), 43830–43837.

22 U. Y. Won, B. H. Lee, Y. R. Kim, W. T. Kang, I. Lee, J. E. Kim, Y. H. Lee and W. J. Yu, Efficient photovoltaic effect in graphene/h-BN/silicon heterostructure self-powered photodetector, *Nano Res.*, 2020, **14**(6), 1967–1972.

23 D. Wu, C. Guo, Z. Wang, X. Ren, Y. Tian, Z. Shi, P. Lin, Y. Tian, Y. Chen and X. Li, A defect-induced broadband photodetector based on WS_2/pyramid Si 2D/3D mixed-dimensional heterojunction with a light confinement effect, *Nanoscale*, 2021, **13**(31), 13550–13557.

24 T. J. Yoo, S. Y. Kim, M. G. Kwon, C. Kim, K. E. Chang, H. J. Hwang and B. H. Lee, A Facile Method for Improving Detectivity of Graphene/p-Type Silicon Heterojunction Photodetector, *Laser Photonics Rev.*, 2021, **15**(8), 2000557.

25 Y. Lu, T. Chen, N. Mkhize, R. J. Chang, Y. Sheng, P. Holdway, H. Bhaskaran and J. H. Warner, GaS:WS_2 Heterojunctions for Ultrathin Two-Dimensional Photodetectors with Large Linear Dynamic Range across Broad Wavelengths, *ACS Nano*, 2021, **15**(12), 19570–19580.

26 Y. Zhou, L. Han, Q. Song, W. Gao, M. Yang, Z. Zheng, L. Huang, J. Yao and J. Li, Hybrid 1D/2D heterostructure with electronic structure engineering toward high-sensitivity and polarization-dependent photodetector, *Sci. China Mater.*, 2022, **65**(3), 732–740.

27 M. Yang, Z. Luo, W. Gao, M. Zhang, L. Huang, Y. Zhao, J. Yao, F. Wu, J. Li and Z. Zheng, Robust Deposition of Sub-Millimeter WSe_2 Drive Ultrasensitive Gate-Tunable 2D Material Photodetectors, *Adv. Opt. Mater.*, 2022, 2200717.

28 J. Chen, Q. Wang, Y. Sheng, G. Cao, P. Yang, Y. Shan, F. Liao, Z. Muhammad, W. Bao, L. Hu, R. Liu, C. Cong and Z. J. Qiu, High-Performance WSe_2 Photodetector Based on a Laser-Induced p–n Junction, *ACS Appl. Mater. Interfaces*, 2019, **11**(46), 43330–43336.

29 W. Zhao, Z. Ghorannevis, L. Chu, M. Toh, C. Kloc, P.-H. Tan and G. Eda, Evolution of electronic structure in atomically thin sheets of WS_2 and WSe_2, *ACS Nano*, 2012, **7**(1), 791–797.

30 Z. Qi, T. Yang, D. Li, H. Li, X. Wang, X. Zhang, F. Li, W. Zheng, P. Fan, X. Zhuang and A. Pan, High-responsivity two-dimensional p-PbI_2/n-WS_2 vertical heterostructure photodetectors enhanced by photogating effect, *Mater. Horiz.*, 2019, **6**(7), 1474–1480.

31 T. H. Tsai, Z. Y. Liang, Y. C. Lin, C. C. Wang, K. I. Lin, K. Suenaga and P. W. Chiu, Photogating WS_2 Photodetectors Using Embedded WSe_2 Charge Puddles, *ACS Nano*, 2020, **14**(4), 4559–4566.

32 G. Kwon, Y.-H. Choi, H. Lee, H.-S. Kim, J. Jeong, K. Jeong, M. Baik, H. Kwon, J. Ahn, E. Lee and M.-H. Cho, Interaction- and defect-free van der Waals contacts between metals and two-dimensional semiconductors, *Nat. Electron.*, 2022, **5**(4), 241–247.

33 Y. Zhou, L. Zhang, W. Gao, M. Yang, J. Lu, Z. Zheng, Y. Zhao, J. Yao and J. Li, A reasonably designed 2D WS_2 and CdS microwire heterojunction for high performance photoresponse, *Nanoscale*, 2021, **13**(11), 5660–5669.

34 W. Wang, Y. Meng, W. Wang, Z. Zhang, P. Xie, Z. Lai, X. Bu, Y. Li, C. Liu, Z. Yang, S. Yip and J. C. Ho, Highly Efficient Full van der Waals 1D p-Te/2D n-Bi_2O_2Se Heterodiodes with Nanoscale Ultra-Photosensitive Channels, *Adv. Funct. Mater.*, 2022, 2203003.

35 Y. T. Lee, P. J. Jeon, J. H. Han, J. Ahn, H. S. Lee, J. Y. Lim, W. K. Choi, J. D. Song, M.-C. Park, S. Im and D. K. Hwang, Mixed-Dimensional 1D ZnO-2D WSe_2 van der Waals Heterojunction Device for Photosensor, *Adv. Funct. Mater.*, 2017, **27**(47), 1703822.

36 D. Hao, D. Liu, S. Zhang, L. Li, B. Yang and J. Huang, Applications of Lead-Free $Cs_2AgBiBr_6$ Single Crystals in Photodetectors and Self-Powered Photodetectors by Symmetric/Asymmetric Electrodes, *Adv. Opt. Mater.*, 2022, **10**(5), 2100786.

37 J. Wu, Z. Yang, C. Qiu, Y. Zhang, Z. Wu, J. Yang, Y. Lu, J. Li, D. Yang, R. Hao, E. Li, G. Yu and S. Lin, Enhanced performance of a graphene/GaAs self-driven near-infrared photodetector with upconversion nanoparticles, *Nanoscale*, 2018, **10**(17), 8023–8030.

38 H. S. Kim, M. Patel, J. Kim and M. S. Jeong, Growth of Wafer-Scale Standing Layers of WS_2 for Self-Biased High-Speed UV-Visible-NIR Optoelectronic Devices, *ACS Appl. Mater. Interfaces*, 2018, **10**(4), 3964–3974.

39 Z. Chen, Z. Zhang, J. Biscaras and A. Shukla, A high performance self-driven photodetector based on a graphene/InSe/MoS_2 vertical heterostructure, *J. Mater. Chem. C*, 2018, **6**(45), 12407–12412.

40 P. Wan, M. Jiang, T. Xu, Y. Liu and C. Kan, High-mobility induced high-performance self-powered ultraviolet photodetector based on single ZnO microwire/PEDOT:PSS heterojunction *via* slight ga-doping, *J. Mater. Sci. Technol.*, 2021, **93**, 33–40.

41 X.-W. Tong, Z.-X. Zhang, D. Wang, L.-B. Luo, C. Xie and Y.-C. Wu, Inorganic $CsBi_3I_{10}$ perovskite/silicon heterojunctions for sensitive, self-driven and air-stable NIR photodetectors, *J. Mater. Chem. C*, 2019, **7**(4), 863–870.

42 M. Zhang, Y. Hu, S. Wang, Y. Li, C. Wang, K. Meng and G. Chen, A nanomesh electrode for self-driven perovskite photodetectors with tunable asymmetric Schottky junctions, *Nanoscale*, 2021, **13**(40), 17147–17155.

43 J. Duan, P. Chava, M. Ghorbani-Asl, Y. Lu, D. Erb, L. Hu, A. Echresh, L. Rebohle, A. Erbe, A. V. Krasheninnikov, M. Helm, Y. J. Zeng, S. Zhou and S. Prucnal, Self-Driven Broadband Photodetectors Based on $MoSe_2$/$FePS_3$ van der Waals n-p Type-II Heterostructures, *ACS Appl. Mater. Interfaces*, 2022, **14**(9), 11927–11936.

44 J. Q. Liu, Y. Gao, G. A. Wu, X. W. Tong, C. Xie, L. B. Luo, L. Liang and Y. C. Wu, Silicon/Perovskite Core-Shell Heterojunctions with Light-Trapping Effect for Sensitive Self-Driven Near-Infrared Photodetectors, *ACS Appl. Mater. Interfaces*, 2018, **10**(33), 27850–27857.

45 Z. Zheng, J. Yao, J. Xiao and G. Yang, Synergistic Effect of Hybrid Multilayer In_2Se_3 and Nanodiamonds for Highly Sensitive Photodetectors, *ACS Appl. Mater. Interfaces*, 2016, **8**(31), 20200–20211.

46 H. Jang, Y. Seok, Y. Choi, S. H. Cho, K. Watanabe, T. Taniguchi and K. Lee, High-Performance Near-Infrared Photodetectors Based on Surface-Doped InSe, *Adv. Funct. Mater.*, 2020, **31**(3), 2006788.

47 X. Zhou, L. Gan, W. Tian, Q. Zhang, S. Jin, H. Li, Y. Bando, D. Golberg and T. Zhai, Ultrathin $SnSe_2$ Flakes Grown by Chemical Vapor Deposition for High-Performance Photodetectors, *Adv. Mater.*, 2015, **27**(48), 8035–8041.

48 Z. Zheng, J. Yao and G. Yang, Centimeter-Scale Deposition of $Mo_{0.5}W_{0.5}Se_2$ Alloy Film for High-Performance Photodetectors on Versatile Substrates, *ACS Appl. Mater. Interfaces*, 2017, **9**(17), 14920–14928.

49 Y. Lu, Y. Wang, C. Xu, C. Xie, W. Li, J. Ding, W. Zhou, Z. Qin, X. Shen and L. B. Luo, Construction of $PtSe_2$/Ge heterostructure-based short-wavelength infrared photodetector array for image sensing and optical communication applications, *Nanoscale*, 2021, **13**(16), 7606–7612.

50 Z. Zheng, J. Yao and G. Yang, Self-Assembly of the Lateral In_2Se_3/$CuInSe_2$ Heterojunction for Enhanced Photodetection, *ACS Appl. Mater. Interfaces*, 2017, **9**(8), 7288–7296.

51 D. Wu, J. Guo, C. Wang, X. Ren, Y. Chen, P. Lin, L. Zeng, Z. Shi, X. J. Li, C. X. Shan and J. Jie, Ultrabroadband and High-Detectivity Photodetector Based on WS_2/Ge Heterojunction through Defect Engineering and Interface Passivation, *ACS Nano*, 2021, **15**(6), 10119–10129.

52 M. Dai, H. Chen, R. Feng, W. Feng, Y. Hu, H. Yang, G. Liu, X. Chen, J. Zhang, C. Y. Xu and P. Hu, A Dual-Band Multilayer InSe Self-Powered Photodetector with High Performance Induced by Surface Plasmon Resonance and Asymmetric Schottky Junction, *ACS Nano*, 2018, **12**(8), 8739–8747.

53 X. Liu, X. Yang, G. Gao, Z. Yang, H. Liu, Q. Li, Z. Lou, G. Shen, L. Liao, C. Pan and Z. Lin Wang, Enhancing Photoresponsivity of Self-Aligned MoS_2 Field-Effect Transistors by Piezo-Phototronic Effect from GaN Nanowires, *ACS Nano*, 2016, **10**(8), 7451–7457.

54 S. Yang, C. Wang, C. Ataca, Y. Li, H. Chen, H. Cai, A. Suslu, J. C. Grossman, C. Jiang, Q. Liu and S. Tongay, Self-Driven Photodetector and Ambipolar Transistor in Atomically Thin GaTe-MoS_2 p–n vdW Heterostructure, *ACS Appl. Mater. Interfaces*, 2016, **8**(4), 2533–2539.

55 W. Wu, Q. Zhang, X. Zhou, L. Li, J. Su, F. Wang and T. Zhai, Self-powered photovoltaic photodetector established on lateral monolayer MoS_2-WS_2 heterostructures, *Nano Energy*, 2018, **51**, 45–53.

56 N. Huo, J. Yang, L. Huang, Z. Wei, S. S. Li, S. H. Wei and J. Li, Tunable Polarity Behavior and Self-Driven Photoswitching in p-WSe_2/n-WS_2 Heterojunctions, *Small*, 2015, **11**(40), 5430–5438.

57 Z. Xie, C. Xing, W. Huang, T. Fan, Z. Li, J. Zhao, Y. Xiang, Z. Guo, J. Li, Z. Yang, B. Dong, J. Qu, D. Fan and H. Zhang, Ultrathin 2D Nonlayered Tellurium Nanosheets: Facile Liquid-Phase Exfoliation, Characterization, and Photoresponse with High Performance and Enhanced Stability, *Adv. Funct. Mater.*, 2018, **28**(16), 1705833.

58 P. Luo, F. Wang, J. Qu, K. Liu, X. Hu, K. Liu and T. Zhai, Self-Driven WSe_2/Bi_2O_2Se van der Waals Heterostructure Photodetectors with High Light On/Off Ratio and Fast Response, *Adv. Funct. Mater.*, 2020, **31**(8), 2008351.

59 Y. Chen, X. Wang, L. Huang, X. Wang, W. Jiang, Z. Wang, P. Wang, B. Wu, T. Lin, H. Shen, Z. Wei, W. Hu, X. Meng, J. Chu and J. Wang, Ferroelectric-tuned van der Waals heterojunction with band alignment evolution, *Nat. Commun.*, 2021, **12**(1), 4030.

60 G. H. Shin, C. Park, K. J. Lee, H. J. Jin and S. Y. Choi, Ultrasensitive Phototransistor Based on WSe_2–MoS_2 van der Waals Heterojunction, *Nano Lett.*, 2020, **20**(8), 5741–5748.